Proceedings of the Seventh International Conference on
Railway Technology: Research, Development and Maintenance
Edited by: J. Pombo
Civil-Comp Conferences, Volume 15, Paper 3.10
Civil-Comp Press, Edinburgh, United Kingdom, 2026
ISSN: 2753-3239, doi: 10.4203/ccc.15.3.10

Elastic Limit for General Elliptical Contacts in Shakedown Diagrams

M. Harake, S. Harake, J. Maierhofer and W. Daves

Department of Simulation, Materials Center Leoben Forschung GmbH, Austria

Abstract

Wear, fatigue, and material deformation are the most common material damages caused by rolling contact fatigue (RCF) in the wheel/rail contact patch. Two important physical quantities in railway engineering, contact pressure and creepage, can be used to predict the material behavior of the wheel/rail contact region. The shakedown map is an important assessment tool used in the railway sector to predict damage caused by RCF. This paper presents a method to calculate the elastic limit of a shakedown map for different wheel/rail contact areas. The study focuses not only on the point and line contacts but also on different elliptical contacts. The focus of this paper is to investigate the influence of different elliptical contact patches on the elastic limit that separates the purely elastic material behavior from the elastic shakedown behavior. Based on an existing Abaqus rollover plugin, a new 3D finite element model representing two-crossed-cylinder is developed to generate elliptical contact areas for continuous rollover simulations. The mentioned model is validated with the Hertzian contact theory. The resulting elastic limit for the point contact is validated with Ponter's analytical solution. The 3D FE model is then used to determine the elastic limits for the rail steel material R350HT, where the semi-axis elliptical ratio of the contact patch is varied.

Keywords: shakedown map, wheel/rail contact, elastic limit, elliptical contact patches, two-crossed cylinders model, finite element simulation

1 Introduction

Rolling contact fatigue failures must be predicted and prevented because they can cause serious accidents. An example is the Hatfield rail crash, which occurred on 17 October 2000 in Hatfield, England. Also, a reason to predict RCF failures is that such failures result in unscheduled maintenances. In railway engineering, the shakedown map is a diagram used to predict wheel and rail damage resulting from RCF.

The inputs for shakedown maps are the applied wheel load onto the rail, the form of the contact patch, and the properties of the used material [6, 10]. The paper by Zhang et al. [2023] [13] shows techniques for predicting when RCF cracks starts. By using shakedown maps, the study identifies the region of crack initiation during rolling contact. It outlines a four-step procedure for calculating crack initiation life. These are: cyclic constitutive model, crack initiation criteria, critical plane analysis, and crack initiation calculation methods. These maps show the boundaries between elastic, elastic shakedown, plastic shakedown, and ratcheting behaviors, which are essential for studying fatigue life and preventing failure in railway components [3]. The application of shakedown theory is important since rolling contact loads are cyclic, which can induce plastic deformation and change rail geometry over time [9]. Ponter's shakedown map have been widely used to predict material failures in rails, but their use is constrained by assumptions such as circular Hertzian contacts [3, 10]. However, real-life situations are often more complicated. Therefore, better methods are needed to include factors like different material properties and changing loads [13]. As a result, researchers are using advanced tools, such as vehicle-track simulations and finite element analysis, to solve these problems. These approaches make shakedown maps more accurate for application in railway operation [3].

The objective of the work by Xie et al. [2023] [12] was to construct a shakedown map for RCF and optimize the classical shakedown map using rolling-sliding twin-disc experiments. To develop this method, specific test parameters, including traction coefficient and contact pressure, were obtained. These experiments were carried out to investigate RCF damage in U75V rail steel. Their primary focus was to develop a more optimized shakedown map by conducting these tests under various contact conditions. Zhou et al. [2025] [14] stated in their paper that standard shakedown maps are useful for predicting RCF, but they often depend on numerical simulations using parameters that do not match real world conditions. The mentioned paper introduced a new 3D shakedown map using finite element analysis and a nonlinear kinematic hardening material model to fix this. They tested how different rail materials (U75V, U71Mn, and U78CrV) affect the shakedown limit. They concluded that traditional shakedown maps give results that are too conservative. In contrast, their new 3D maps provide more accurate, higher limits, making them a better tool for predicting rail wear and fatigue.

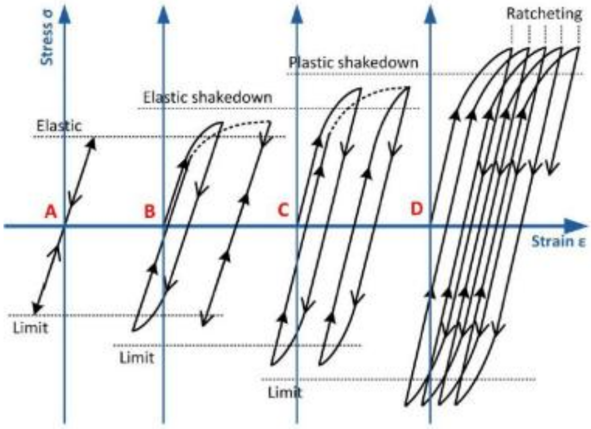

Figure 1: Material responses: A) purely elastic response, B) elastic shakedown response, C) plastic shakedown response, D) ratcheting response [1, 8].

Figure 1 shows the four material responses to cyclic loading, first studied by Bower and Johnson [1989] [1]. When a material is subjected to cyclic loading, it can respond in four different ways, which are based on the magnitude of the stress caused by the external loads. In the elastic region, the material stays within its limits, the yield strength, and always returns to its original geometry. During elastic shakedown, the material deforms at first, but it stops changing after a few cycles and begins acting purely elastically again. In the plastic shakedown region, the deformation stabilizes after some time, but the material continues experience plastic deformation but in a steady hysteresis loop. Finally, ratchetting occurs when the material keeps deforming more and more during every cycle until it fails.

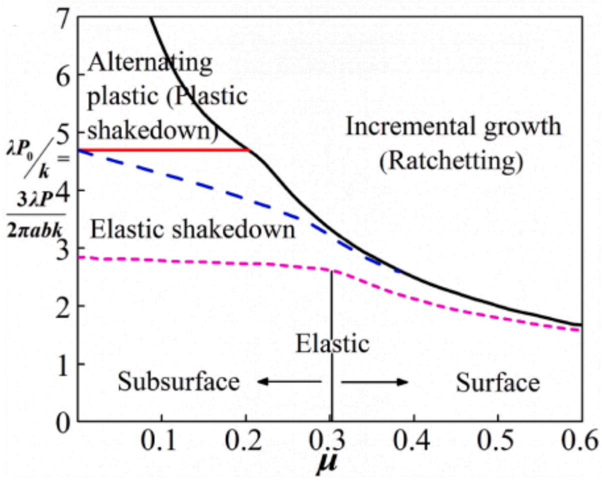

Figure 2: Classical shakedown diagram for full slip condition in point contact according [5, 10, 12].

The four states depend on three main parameters: the maximum contact stress P_0, the shear yield strength (see Equation 1, where σ_y represents the tensile yield strength), and the traction coefficient μ (see Equation 3, where F_t represents the tangential force and F_n represents the normal force, both acting on the contact patch). To develop a classical shakedown map, these three parameters must be determined. The traction coefficient is placed on the x-axis, while the y-axis shows the $normalized\ vertical\ load$ (see Equation 2), which is calculated by dividing the maximum contact stress by the shear yield strength. According to the paper by Ponter et al. [1985] [10], λ is defined as the load factor, P_0 is the maximal Hertzian pressure under load F, and k_e represents the yield stress in simple shear, with P_0/k_e is the non-dimensional applied load ratio. This study focuses specifically on the elastic limit, which is the boundary between purely elastic behavior and elastic shakedown. The intention of this work is the development of the elastic limits for various elliptical contacts.

$$k_e = \frac{\sigma_y}{\sqrt{3}} \tag{1}$$

$$normalized\ vertical\ load = \frac{P_0}{k_e} \tag{2}$$

$$\mu = \frac{F_t}{F_n} \tag{3}$$

1.1 Hertzian Contact Theory

Hertzian contact theory is a theory used to explain how elastic parts deform when pressed together. The theory classifies the resulting contact area as a point, elliptical, or line contact. The material is assumed to be elastic, isotropic, and homogeneous. Only small deformations take place at the contact patch, which is small in dimension compared to the contacting parts [4]. According to Kunz J. [2009] [7], the equations of the Hertzian contact theory for crossed cylinders, where the intersecting angle is 90°, are as follows.

$$p_{max} = 0.364\,(1-\chi^2)^{0.2}\sqrt[3]{\frac{F}{R_V^2}\left(\frac{E_V}{1-\nu_V^2}\right)^2}\ \ldots\ Normal\ contact\ pressure \tag{4}$$

By applying the equation above, one can calculate the vertical load required to achieve a specific contact pressure.

$$F = \left(\frac{p_{max}}{0.364\,(1-\chi^2)^{0.2}}\right)^3\left(\frac{R_V\,(1-\nu_V^2)}{E}\right)^2\ \ldots\ Vertical\ load \tag{5}$$

The semi-axes a and b of the elliptical Hertzian contact area can be calculated using equations 6 and 7.

$$a = 1.15\,(1-\chi^{0.64})^{-0.4}\sqrt[3]{F\,R_V\,\frac{1-\nu_V^2}{E_V}}\ \ldots\ Major\ elliptical\ axis \tag{6}$$

$$b = 1.15\,(1-\chi^{0.5})^{0.25}\sqrt[3]{F\,R_V\,\frac{1-\nu_V^2}{E_V}} \; \ldots \; Minor\ elliptical\ axis \tag{7}$$

In equations 4-7, $\chi = \left|\frac{R_{upper}-R_{lower}}{R_{upper}+R_{lower}}\right|$ represents the geometric factor. The terms $R_V = 2\,\frac{R_{upper}\,R_{lower}}{R_{upper}+R_{lower}}$, $E_V = 2\,\frac{E_{upper}\,E_{lower}}{E_{upper}+E_{lower}}$ and $\nu_V = \sqrt{\frac{E_{upper}\nu_{upper}^2+E_{lower}\nu_{lower}^2}{E_{upper}+E_{lower}}}$ represent the equivalent radius, equivalent elastic modulus, and equivalent Poisson's ratio, respectively. In the case where the upper and lower cylinders have similar elastic properties, it can be assumed that $E_V = E$ and $\nu_V = \nu$. The results of these equations are used in this study to validate the simulation results.

2 Methods

This section briefly describes the modified model by Gapp et al. [2025] [2], which is based on the original Abaqus rollover Plugin by Meyer et al. [2021] [9]. In the original and modified models, the upper cylinder (representing the wheel) is modeled using super-elements. Consequently, it cannot be assigned an elastic-plastic material definition.

Since plasticity is essential for creating the shakedown map of the wheel material, a new fully 3D model is introduced. This new model is designed to generate shakedown maps for both the rail and wheel materials. However, the current work focuses specifically on determining the elastic limit of the rail material for point, line, and various elliptical contacts. The procedure for this determination is illustrated in the flowchart below.

2.1 Extended Abaqus Rollover Plugin

The extended Abaqus rollover plugin, illustrated in *Figure 4*, in which a wheel continuously rolls over a rail, simulates cyclic elasto-plastic Hertzian contact in wheel/rail interactions. By simplifying the wheel/rail geometries into two crossed cylinders (as illustrated in *Figure 3*), the model generates various contact shapes, including point, line, and elliptical patches. These shapes are controlled by varying the radius of the lower cylinder, while the upper cylinder radius remains fixed at 460 mm, in accordance with Hertzian theory. This modification significantly reduces the computation time required for the large number of rollovers needed to calculate incremental plastic strains, which distinguish between elastic shakedown, plastic shakedown, and ratcheting.

The work by Gapp et al. [2025] [2] aimed to analyze cyclic rolling contact in wheel/rail interactions, focusing on understanding cyclic plastic deformation specifically in the rail. Therefore, only the lower cylinder was assigned an elastic-plastic material behavior. The upper cylinder in the extended Abaqus rollover plugin was modeled using super-elements, which cannot be assigned an elastic-plastic material behavior. With the aim of developing shakedown maps for the wheel (in addition to the rail) in the future, the upper cylinder is modeled as a 3D part in this work, allowing for the assignment of elastic-plastic material behavior.

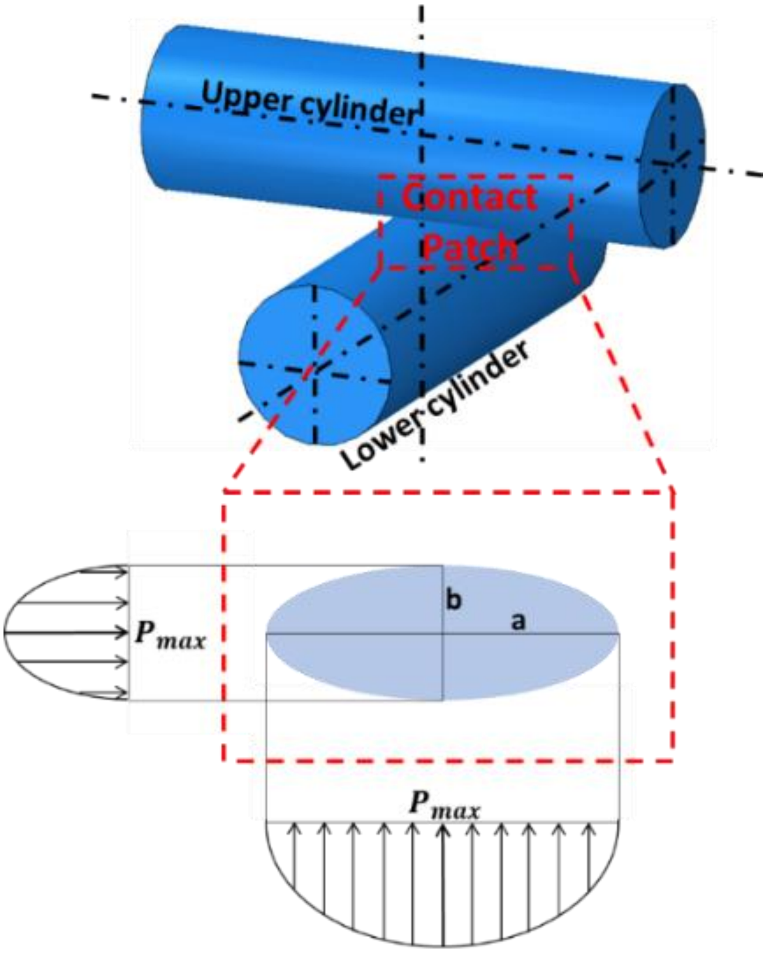

Figure 3: (a) Full two crossed cylinders. (b) Resulting contact patch according to Hertzian theory (ideal conditions)

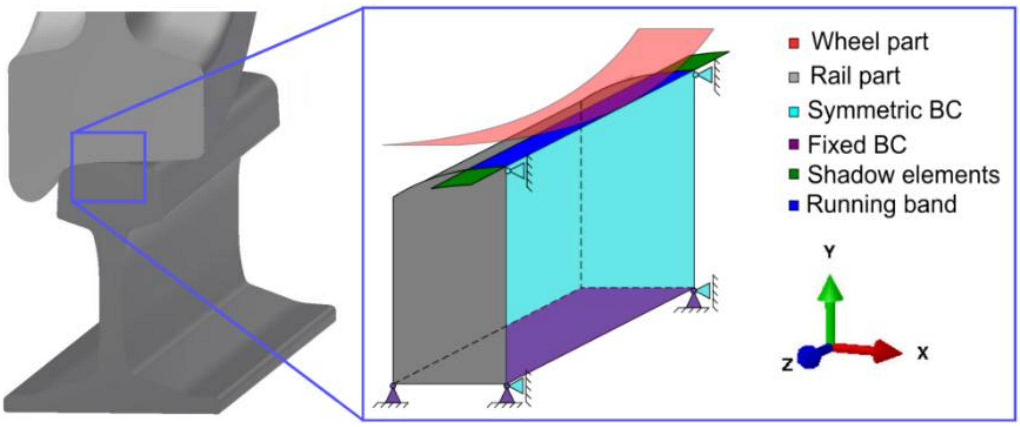

Figure 4: Modified FE-model: Wheel/rail parts, applied boundary conditions (BCs), super-elements, shadow elements

2.2 Three dimensional crossed-cylinder model

The current 3D crossed-cylinder model (Figure *6*) is based on the extended Abaqus rollover plugin. The model consists of cutout sections of the upper and lower cylinders, representing the wheel and rail, respectively. The model is generated by a fully automated Abaqus Python script, enabling parametric studies to be performed.

The geometrical parameters of the two cylinders are listed in *Table 1* and illustrated in *Figure 5*. By selecting specific rail and wheel radii, the desired semi-axis ratios (b/a) can be simulated. Symmetry boundary conditions are applied to both cylinders in the XY-plane, and the rail cylinder is fixed at the bottom surface. The boundary conditions are illustrated in *Figure 5*. The rolling direction is in the positive X-direction.

Table 1: Geometrical parameters of the 3D crossed-cylinder model

Geometrical Parameter	**Symbol**	**Value**
Rail radius	R_{rail} [mm]	35, 109, 222, 363 and 460
Rail width	W_{rail} [mm]	40.0
Rail height	H_{rail} [mm]	42.25
Rail length	L_{rail} [mm]	36.0
Wheel radius	R_{wheel} [mm]	460.0
Wheel inner radius	$R_{i,wheel}$ [mm]	417.75
Cutout-section of the wheel	α_{cutout} [°]	5.082

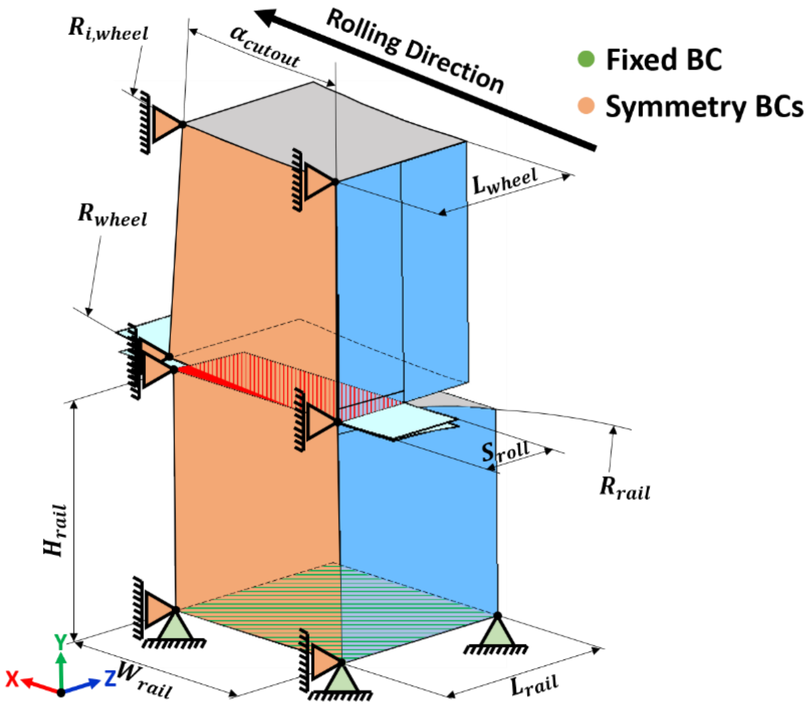

Figure 5: Geometry and applied boundary conditions of the wheel and rail parts

While the rail geometry remains unchanged from the plugin, both the shadow elements (depicted in light blue) and the rail part are discretized using C3D8R elements (eight-node hexahedral elements with reduced integration). Furthermore, the wheel geometry, originally modeled using super-elements, is now modeled as a full 3D part, also utilizing C3D8R elements. The surface elements of the running band (depicted in red) and the shadow elements have a length of $0.25\,mm$ in the rolling direction. To ensure the narrowest elliptical contact patch is captured, a biased mesh is applied in lateral direction, reducing the minimum element size to $0.25\,x\,0.016\,mm$. Periodic boundary conditions are applied to the front and back faces (highlighted in blue) of both the wheel and rail, as well as between the shadow elements at the beginning and end of the contact, to simulate continuous rolling. The periodic coupling of the corresponding nodes is illustrated in Figure *7*. The normal contact behavior between the cylinders is defined using a hard contact pressure-overclosure relationship enforced by the linear penalty method with the default contact stiffness. The tangential contact behavior is defined using a penalty friction formulation, with the coefficient of friction varied from 0 to 0.6. The slip tolerance, from which the elastic slip is calculated, is set to 0.001 [-] (Default value is 0.005 [-]) to increase the accuracy of the solution.

The rotational displacement $\vec{\theta}^w$ of the wheel about the Z-axis is controlled by a reference point, which is coupled to the inner surface of the wheel and located at the center of the upper cylinder. The translational displacement $\vec{U}^r$ of the rail is applied to the lower surface in the X-direction. A vertical wheel load $\vec{F}^w$ is applied to the reference point in the negative Y-direction during rolling. Longitudinal creepage is induced by the difference between the longitudinal displacement $\vec{U}^r$ of the rail and the circumferential displacement $R_{wheel} \cdot \vec{\theta}^w$ of the wheel.

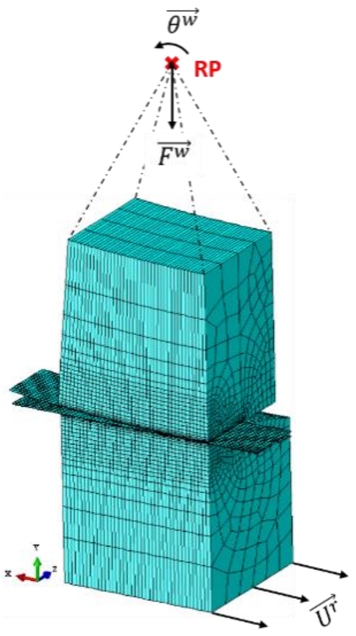

Figure 6: 3D crossed cylinders FE-model

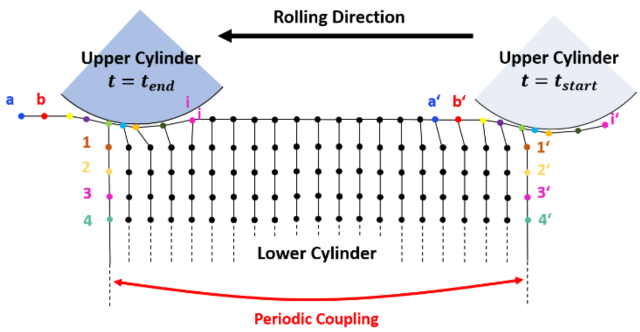

Figure 7: Periodic boundary conditions defined at the symmetry face of the rail

As the purpose of this study is to determine the elastic limit, an elastic material model is used, defined by the elastic modulus and Poisson's ratio. The material properties for the rail grade R350HT are listed in *Table 2*, with the parameters taken from the paper by Velic et al. [2023] [11].

Table 2: Material properties of R350HT rail grades

Material parameter	**R350HT**
Young's elastic modulus E [GPa]	206.0
Poisson's ratio ν [$-$]	0.3
Yield strength σ_y [MPa]	340.0

2.3 Procedure to determine the elastic limit

For classifying whether the material starts yielding, the von Mises yield criterion was used. To determine the elastic limit for full slip conditions ($\mu = COF$), which is reached by setting the creepage to approximately 2.5 %, the friction coefficient (COF) is first set to a fixed value, and the wheel load (F_{wheel}) applied to the upper cylinder is assigned a value. These parameters are input into an Abaqus Python script to generate the model. For the elastic limit determination, the simulations are performed for a single cycle ($N = 1$). In post-processing, the von Mises stress (σ_{vM}), maximum contact pressure (p_0), and the normal (F_n) and tangential (F_t) forces acting on the contact patch are extracted. From these values, the normalized vertical load (p_0/k_e) and the traction coefficient (μ) are calculated. Subsequently, if the von Mises yield criterion is not satisfied, the load applied to the upper cylinder is adjusted using the Hertzian contact relation for axisymmetric bodies (see Equation 4). This relation states that the stresses are proportional to the cube root of the load, from which the next load magnitude is derived. The model is then updated with the newly calculated force, regenerated, and the simulation is executed again. This procedure is repeated until the absolute difference between the maximum von Mises stress and the yield strength falls within a specified tolerance ($|\sigma_{vM} - \sigma_y| < tolerance$). Once the elastic limit for a specific COF is determined, the corresponding data point (p_0/k_e, μ) is stored and the current simulation loop ends. The process then starts for the next COF increment.

$$\sigma \propto F^{1/3} \qquad \Leftrightarrow \qquad F_{i+1} = F_i \cdot \left(\frac{\sigma_y}{\sigma_i}\right)^3 \tag{4}$$

The automated procedure for determining the elastic limit is illustrated in the following flowchart:

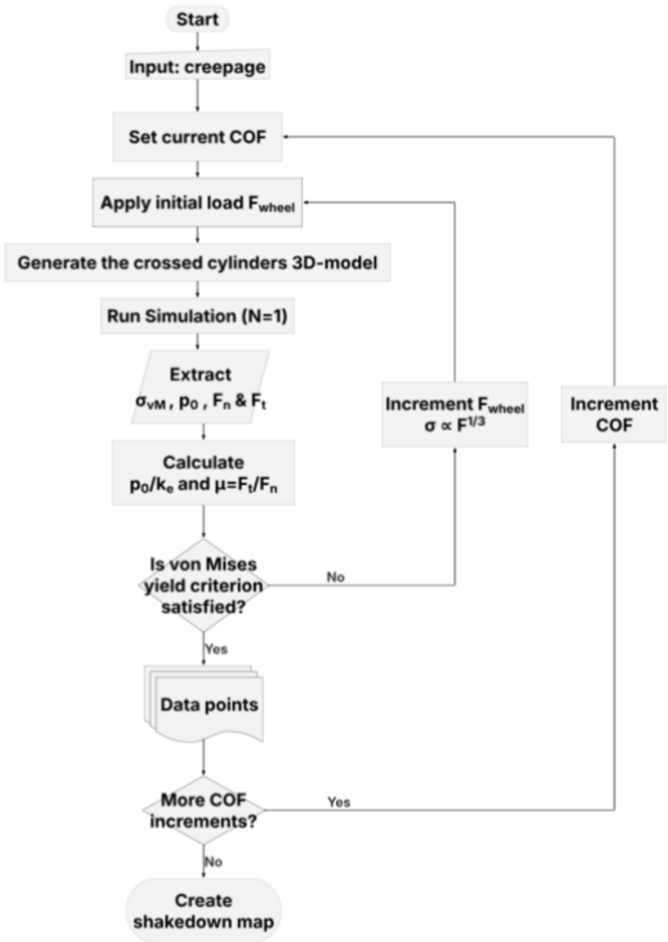

Figure 8: Flowchart for determining the elastic limit

3 Results

The model is validated in two steps. First, the results are compared against Hertzian analytical solutions (Equations 4-7), and second, the simulated point contact ($b/a = 1.0$) elastic limit is compared with analytical solution from Ponter et al. [1985] [10]. These results are presented in *Table 3* and *Figure 9*, respectively.

The simulation results show that there is satisfactory agreement with the analytical Hertzian solutions for point, elliptical, and near-line contacts (corresponding to semi-axis ratios of 1.0, 0.6, and 0.2, respectively). The highest relative errors for the contact semi-axes a and b are observed in the model where $b/a = 0.2$. These discrepancies could be reduced by further refining the mesh in the contact area. The simulated elastic limit for point contact shows good agreement with Ponter's analytical solution for $\mu < 0.3$. The slight deviations that occur for $\mu > 0.3$ can be minimized by further mesh refinement.

Table 3: Comparison between Hertzian theory and the FE model

Parameter	Hertz results			Simulation results			Relative error [%]		
R_{rail} [mm]	460	222	35	460	222	35	−	−	−
p_{max} [MPa]	539.3	552.4	615.2	549.8	569.3	598.4	+1.94	+3.06	−2.72
a [mm]	3.463	3.152	1.887	3.521	3.135	2.034	+1.68	−0.54	+7.79
b [mm]	3.463	1.895	0.380	3.568	1.931	0.404	+3.03	+1.90	+6.32
b/a [−]	1.0	0.6	0.2	1.013	0.616	0.199	+1.30	+2.67	−0.50

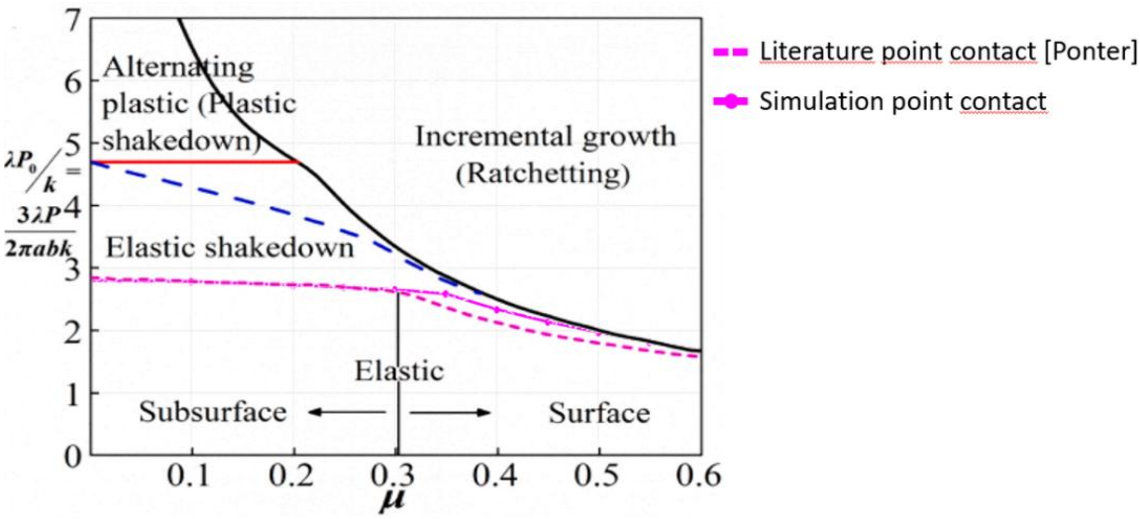

Figure 9: Validation of the FE-model for point contact against Ponter's analytical solution

By varying the rail radius, general elliptical contacts are generated. The elastic limit curves for these patches under full slip conditions ($\mu = COF$), illustrated in *Figure 10*, are constructed using the method described in Section 2.3. The resulting curves exhibit similar behavior as the traction coefficient increases, with the elastic limits for elliptical contacts falling between the those of point and line contacts.

The actual calculations show some difference to the analytical solutions for a traction coefficient bigger 0.3. Actual studies show that using a refined mesh the difference approaches zero. The results will be updated as soon as the computation of the new results with the refined mesh is finished.

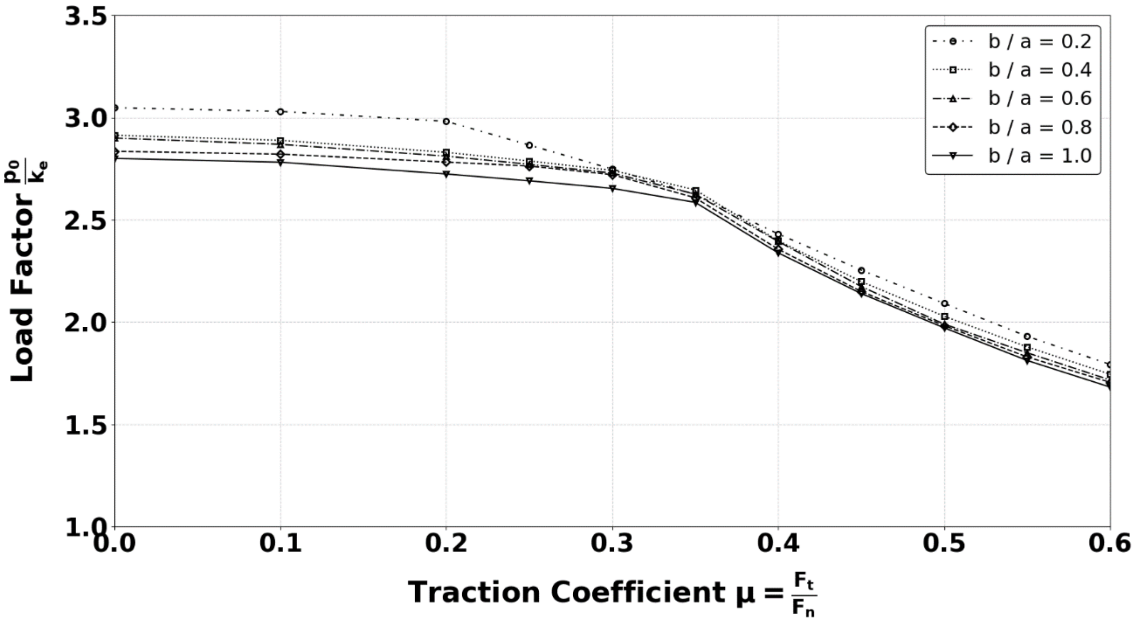

Figure 10: Elastic limits of R350HT for general elliptical contact patches

4 Conclusion

- Development of an efficient 3D FE model to analyze the elastic limits of general elliptical contacts within the shakedown map.
- Simulation results show satisfactory agreement with analytical Hertzian solutions for general elliptical contacts.
- The simulated elastic limit for point contact agrees well with Ponter's analytical solution. However, with further mesh refinement, the results will be strongly improved.
- The plotted curves of the elastic limits for general elliptical contacts demonstrate a similar trend with increasing traction coefficients.
- As expected, the elastic limits for general elliptical contacts are located between the extreme cases of point and line contacts.

Acknowledgements

The authors gratefully acknowledge the financial support under the scope of the COMET program within the K2 Center “Integrated Computational Material, Process and Product Engineering (IC-MPPE)” (Project No 886385). This program is supported by the Austrian Federal Ministries for Economy, Energy and Tourism (BMWET) and for Innovation, Mobility and Infrastructure (BMIMI), represented by the Austrian Research Promotion Agency (FFG), and the federal states of Styria, Upper Austria and Tyrol.

References

[1] A. F. Bower and K. L. Johnson. 1989. The influence of strain hardening on cumulative plastic deformation in rolling and sliding line contact. *Journal of the Mechanics and Physics of Solids* 37, 4, 471–493. DOI: https://doi.org/10.1016/0022-5096(89)90025-2.

[2] S. Gapp, D. Otipka, J. Maierhofer, W. Daves, and T. Antretter. 2025. Efficient 3D finite element modeling of elasto-plastic Hertzian contact of two crossed cylinders with varying contact ellipses after high cycles. *Tribology International* 211, 110825. DOI: https://doi.org/10.1016/j.triboint.2025.110825.

[3] S. J. Hawksbee, G. J. Tucker, and M. Burstow. 2020. Use of shakedown maps to assess plastic flow in railway curves. *Proceedings of the Institution of Mechanical Engineers, Part F: Journal of Rail and Rapid Transit* 234, 4, 417–425. DOI: https://doi.org/10.1177/0954409719881518.

[4] H. R. Hertz. 1882. Über die Berührung fester elastischer Körper und Über die Härte. *Verhandlungen des Vereins zur Beförderung des Gewerbefleisscs, Berlin: Verein zur Beförderung des Gewerbefleisses*, 449–463.

[5] Hills D. A., Nowell D., and Sackfield A. 1993. *Mechanics of Elastic Contacts*. Butterworth-Heinemann.

[6] K. L. Johnson. 1989. The Strength of Surfaces in Rolling Contact. *Proceedings of the Institution of Mechanical Engineers, Part C: Journal of Mechanical Engineering Science* 203, 3, 151–163. DOI: https://doi.org/10.1243/PIME_PROC_1989_203_100_02.

[7] Kunz J. 2009. Kontaktprobleme und ihre praktische lösung. *Konstruktion, Zeitschrift für Produktentwicklung und Ingenieur-Werkstoffe*, 54–58.

[8] Meghoe A., Jamshidi A., Leondersloot R:, Tinga T. TOWARDS THE DEVELOPMENT OF A HYBRID METHODOLOGY FOR MONITORING OF HEAD CHECKS IN RAILWAY INFRASTRUCTURE. *15th international conference on railway engineering* 2019, pp. 1-12.

[9] K. A. Meyer, R. Skrypnyk, and M. Pletz. 2021. Efficient 3d finite element modeling of cyclic elasto-plastic rolling contact. *Tribology International 161: 107053. DOI: https://doi.org/*10.1016/j.triboint.2021.107053.

[10] A.R.S. Ponter, A. D. Hearle, and K. L. Johnson. 1985. Application of the kinematical shakedown theorem to rolling and sliding point contacts. *Journal of the Mechanics and Physics of Solids* 33, 4, 339–362. DOI: https://doi.org/10.1016/0022-5096(85)90033-X.

[11] D. Velic, M. Krobath, E. Stocker, U. Ossberger, J. Gsodam, and W. Daves. 2023. A finite element modelling approach for the numerical analysis of switch rail contact loading and cyclic profile degradation. *Proceedings of the Institution of Mechanical Engineers, Part F: Journal of Rail and Rapid Transit* 237, 2, 157–165. DOI: https://doi.org/10.1177/09544097221095694.

[12] Y. Xie, W. Wang, J. Guo, B. An, R. Chen, Q. Wu, E. Bernal, H. Ding, and M. Spiryagin. 2023. *Rail rolling contact fatigue response diagram construction and shakedown map optimization*, 528-529.

[13] S. Zhang, Q. Liu, M. Spiryagin, Q. Wu, H. Ding, Z. Wen, and W. Wang. 2023. Gaps, challenges and possible solution for prediction of wheel–rail rolling contact fatigue crack initiation. *Rail. Eng. Science* 31, 3, 207–232. DOI: https://doi.org/10.1007/s40534-023-00302-8.

[14] Z. Zhou, C. Yang, G. Tao, and Z. Wen. 2025. *A Finite Element Method for Reconstruction of Shake-Down Map in Wheel–Rail Rolling–Sliding Contact*.